Materials for life sciences

Check for updates

Tuning the mechanical, microstructural, and cell adhesion properties of electrospun ε-polycaprolactone microfibers by doping selenium-containing carbonated hydroxyapatite as a reinforcing agent with magnesium ions

M. K. Ahmed[1,*] , S. F. Mansour[2], Reem Al-Wafi[3], S. I. El-dek[4], and V. Uskoković[5]

[1] Department of Physics, Faculty of Science, Suez University, Suez, Egypt

[2] Physics Department, Faculty of Science, Zagazig University, Zagazig, Egypt

[3] Physics Department, Faculty of Science, King Abdulaziz University, Jeddah, Saudi Arabia

[4] Materials Science and Nanotechnology Department, Faculty of Postgraduate Studies for Advanced Sciences, Beni-Suef University, Beni Suef, Egypt

[5] Department of Mechanical and Aerospace Engineering, University of California, Irvine, CA 92697, USA

ABSTRACT

The flexible lattice of hydroxyapatite (HAP) allows for doping with ions widely varying in size and charge and these ions can impart a range of properties that could be harnessed for high technology applications. However, incorporation of combinations of ions, each of which endows HAP with different properties, has rarely been explored, let alone in combination with polymers. Carbonated hydroxyapatite (CHAP) dually doped with magnesium and selenite ions (Mg–Se–CHAP) was synthesized at different contents of the Mg^{2+} dopant and integrated within electrospun ε-polycaprolactone (PCL) microfibers. The formula $Mg_xCa_{(10-x)}(PO_4)_{5.8}(SeO_2)_{0.2}(OH)_2$ represented the ceramic component of Mg–Se–CHAP/PCL fibers, whose properties were studied for different values of the stoichiometric parameter x in the $0.0 \leq x \leq 0.5$ range. The structural investigation indicated that the lattice parameter *a* decreased with the addition of Mg^{2+} from $x = 0$ to $x = 0.3$, at which point it reached its minimal value of 9.414 Å, while the lattice parameter *c* increased with the addition of Mg^{2+} from $x = 0$ to $x = 0.3$, at which point it reached its maximal value of 7.050 Å. The morphological properties depended strongly on the Mg^{2+} content, as the fibrous scaffolds became more networked, rougher on the surface, and less porous with the addition of Mg^{2+}. All of these surface properties affected the human fibroblastic HFB4 cell response to these materials. While the cell viability tests indicated a

Address correspondence to E-mail: mkaa@zu.edu.eg

perfectly safe response toward the cells after 3 days of exposure, the cell adhesion, and proliferation improved upon the addition of Mg^{2+} to the Se–CHAP phase, and infiltration into surface pores varied, again as a function of the Mg^{2+} content. The mechanical properties were also strongly affected by the Mg^{2+} concentration, with tensile strength, fracture toughness and elastic modulus all recording their highest values for the $x = 0.2$ composition, typically being a dozen times higher than the values recorded for the Mg^{2+}-free, $x = 0.0$ composition. These results show that a range of composite scaffold properties combining a polymer as the main phase (88 wt%) and HAP as the secondary phase (12 wt%), including the microstructural, mechanical and biological, can be tuned by controlling a relatively subtle and inconspicuous compositional parameter—the content of the Mg^{2+} dopant incorporated in the structure of HAP. Despite the low content of this ion in the dually doped CHAP/PCL microfibrous matrix, ranging between the Mg^{2+}/Ca^{2+} molar ratios of 1:100 and 1:20, the high dependency of the material properties on the concentration of Mg^{2+} suggests that this approach may warrant further investigation for potential clinical applications.

Introduction

In the USA alone, close to 44 million people, representing more than 50% of the population over 50 years of age, live with osteoporosis, a systemic disease that often leads to fractures and requires multiple surgeries [1]. Osteomyelitis, osteosarcoma, injuries due to trauma, genetic skeletal malformations and other diseases further contribute to the cases necessitating bone surgery. Therefore, there is a high requirement for biomaterials that can rehabilitate bone tissue after injuries, infections, physical damage, osteoporosis, or tumor resection. Compared to the common bone substitutes of the day, there is a room for enhancing the quality of bone grafts to meet the clinical requirements, which naturally crave biomaterials as similar to the biological and mechanical properties of bone as possible. Due to their biocompatibility and osteoconductivity, ceramic bone grafts have attracted continuous attention ever since the word "biomaterials" was coined in the 1970s [2]. Hydroxyapatite (HAP) is one of the most commonly studied bioceramics because of its resemblance to the mineral part of human hard tissues, whose main constituents are biogenic apatite and collagen fibers [3, 4].

Despite this commonality, HAP suffers from comparatively high brittleness and low fracture toughness, which both restrict its utilization under high load bearings. The fracture toughness, K_c, of HAP is only 1 MPa m$^{1/2}$, which is much lower than the K_c of bone [5], equaling around 6.4 and 5.1 for human femur in the transverse and longitudinal directions, respectively [6, 7]. As a matter of fact, one way by which the bone mineral compensates for the high brittleness and low fracture toughness of HAP is by lowering the particle dimensions down to the nanoscale, so that the fracture stresses become relatively high [8]. Reinforcement of HAP by combining it with appropriate polymers, albeit without diminishing the biological characteristics of HAP, has thus grown into a mainstream strategy in the tissue engineering field. The bone itself is one such natural composite whose mineral part, HAP, is embedded directionally in an organic matrix composed mainly of collagen fibers.

HAP ($Ca_{10}(PO_4)_6(OH)_2$) crystallizes in a hexagonal symmetry with $P6_3/m$ space group where $a = 9.432$ Å and $c = 6.881$ Å. It consists of 10 Ca positions, four of which are classified as Ca(1) and six as Ca(2), in addition to six tetrahedral (PO_4^{3-}) sites and two $(OH)^-$ ones in the screw axis channels. One of the most essential characteristics of the HAP lattice is its structural flexibility. In other words, Ca sites could be replaced by a plethora of cations, such as Na^+, K^+, Ag^+, Fe^{2+}, Mg^{2+}, Cu^{2+}, Zn^{+2}, Sr^{+2}, Cd^{+2}, Bi^{3+}, La^{3+}, Y^{3+}, Al^{3+}, and Zr^{4+}, while (PO_4^{3-}) may be exchanged with (CO_3^{2-}), (SeO_3^{2-}) and (SiO_4^{4-}), and F^- and Cl^- may substitute $(OH)^-$ positions [5, 9, 10]. However, to keep the neutrality of a HAP crystal, if a monovalent ion replaces one of the Ca sites, a supplementary

vacancy would be created. As such substitutions increase in frequency, so does the concentration of lattice voids increase too, further increasing the propensity of HAP to accommodate other ionic dopants within the limits of preservation of its space group symmetry. In addition, Ca(2) volume is somewhat larger than Ca(1), as the result of which larger cations are more prone to replace Ca(2), with the caveat that the ionic replacements are more strongly dependent on the charge density than on the ionic radii [5].

Magnesium is one of the most commonly investigated cationic substitutes in HAP. The deficiency of Mg^{2+} in natural bone is strongly associated with osteoporosis [11]. It is reported that the Mg^{2+} content in natural enamel is around 0.44 wt%, while in dentin it reaches 1.23 wt% [9]. Regarding the lattice effects of $Ca^{2+} \rightarrow Mg^{2+}$ substitution, the accommodation of Mg^{2+} ion into one of the Ca sites induces a contraction of the unit cell c-axis due to the smaller ionic radius of Mg^{2+} (0.69 Å) compared to the Ca^{2+} ion (0.99 Å). A number of prior studies explored the effects of the addition of Mg^{2+} to HAP, starting from the work from 1971 by Neuman and Mulryan [12]. Tomazic et al. were also among the first to study the incorporation of Mg^{2+} into HAP [13], and these early studies were focused more on the chemical and microstructural effects on Mg^{2+} incorporation. In contrast, the interest of more recent studies has been primarily to evaluate the biological responses to Mg–HAP. The first study to test the response of bone cells to Mg–HAP was by Serre et al., and it demonstrated a toxic effect in human osteoblasts [14]. Both toxicity and the inhibition of mineralization were induced in direct proportion with the concentration of Mg^{2+} ions in Mg–HAP. However, reiterating the findings of solid osteoconductivity of Mg-substituted tricalcium phosphate in a rat femoral model reported in 2007 [15], Landi et al. [16] reported in 2008 an increase in osteoconductivity and the resorption rate of Mg–HAP in a rabbit femoral bone model compared to Mg-free HAP. A number of subsequent studies confirmed this augmented osteoconductivity of Mg–HAP compared to pure HAP [17]. Above specific concentration thresholds, Mg^{2+} in Mg–HAP also starts to exert pronounced antibacterial activities [18], and the effect was shown to be associated with the modification of the topography and electrostatic characteristics of the particles following $Ca^{2+} \rightarrow Mg^{2+}$ substitution [19]. Because of its positive

in vitro and in vivo response, Mg-doped HAP has found its way to cell-seeded biomimetic scaffolds in combination with collagen [20], chitosan [21] and other polymers.

Concerning the anionic substitutions, it should be mentioned that natural HAP is doped with (CO_3^{2-}) at the content of around 7 wt%, where this ion has two possible positions to occupy, namely A-type $[(CO_3^{2-}) \rightarrow (OH)^-]$ and B-type $[(CO_3^{2-}) \rightarrow (PO_4^{3-})]$, whereas their mixture is classified as AB-type $[(CO_3^{2-}) \rightarrow (PO_4^{3-})$ and $(OH)^-]$. The incorporation of carbonate increases the biodegradation rate due to the weaker bonding of Ca^{2+} to (CO_3^{2-}) than of Ca^{2+} to (PO_4^{3-}).

Selenium exists in the human body as a trace element, where it acts as an antioxidant by hindering the action of free radicals as metabolic by-products in cells [22]. Selenium, in addition, may act as an anticarcinogenic agent and has been investigated for its role in the inhibition of cancer cell proliferation [23, 24]. It was reported that selenium deficiency may reduce the bone strength and be accompanied by the inhibition of bone growth [25]. In addition to this, the incorporation of HAP doped with selenite into a bone defect in situ may inhibit the recurrent tumorogenesis in that very same spot [25]. Selenium may be also utilized as an agent that protects the organism from cardiovascular disease [26] and is approved by the US Food and Drug Administration (FDA) to be used as a daily dietary supplement [27].

The divalent, (SeO_3^{2-}) anion adopts a flat, trigonal pyramidal shape with the radius of 2.38 Å, while (PO_4^{3-}) assumes a tetrahedral shape with the radius of 2.39 Å. Notwithstanding the similarity in size, this difference in geometry exerts a considerable influence on the crystallographic effects of the $(PO_4^{3-}) \rightarrow (SeO_3^{2-})$ ionic substitution [28]. Regarding prior work on selenite-substituted HAP, Wang et al. [27] utilized a waste eggshell to synthesize selenite-doped HAP (Se–HAP) by co-precipitation and hydrothermal processing, thus obtaining uniform nanorods with the length of around 50 nm and the width of 6 nm. Wei et al. [29] studied the crystal structure effects of doping HAP with (SeO_3^{2-}) and showed that the lattice strain increases with the dopant concentration, while the mean particle sizes decrease. Also, the lattice parameter a increases, while the lattice parameter c decreases [29].

Single ionic substitutions exert definite effects on the structure and properties of HAP, but their synergies can further affect the HAP lattice and may have a significant effect on its behavior in biological environments. Wei et al. [3] investigated the co-substitution of Ca^{2+} and (PO_4^{3-}) sites with Sr^{2+} and (SeO_3^{2-}), respectively, and found out that the lattice parameters a and c both expanded, along with the unit cell volume. On the other hand, Szurkowska et al. [9] introduced Mg^{2+} and (SiO_4^{4-}) as co-substitutes into HAP at 0.26 wt% and 0.59 wt %, respectively, and observed no significant variation of crystallographic parameters, meaning that the two dopants most probably compensated for the effects of each of them alone. Luo et al. [10] also designed lamellar nanoparticles of HAP co-doped with (SeO_3^{2-}) and Gd^{3+} and demonstrated that this dual doping enhances the biocompatibility of HAP, while also allowing it to display magnetic and photoluminescent properties. One thing is certain, though: no combinations of ionic substitutes could improve significantly on the aforementioned mechanical weaknesses of HAP and render it available for load-bearing applications. Therefore, other approaches are needed to compensate for this fundamental issue. Inspired by the natural bone design mentioned earlier, where lowly crystalline carbonated HAP (CHAP) is directionally dispersed along collagen fibers, here we follow a biomimicry approach by incorporating multi-doped HAP, containing Mg^{2+}, (SeO_3^{2-}) and (CO_3^{2-}) as dopants, into microfibrous polymeric scaffolds.

One of the most attractive polymers investigated for biomedical applications is ε-polycaprolactone (PCL). Its attractiveness to the medical field stems from its biocompatibility, its adequate tensile strength, solid processibility, low cost and, finally, the fact that it has already been approved by the FDA. Bose et al. [1] investigated the influence of PCL on the release of alendronate from Mg–HAP coated on a Ti substrate and found out that PCL could inhibit the burst release of the drug and initiate its controlled, sustained release. Also, Gorodzha et al. [30] studied the biological effects of incorporating (SiO_4^{4-})-doped HAP within PCL nanofibers and showed that the differentiation of human mesenchymal stem cells occurs in the osteogenic direction. Meanwhile, Torres
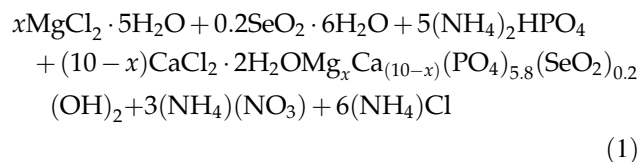
et al. [31] investigated the effect of halloysite combined with HAP at the content of 20 wt% and a fixed ratio of PCL as a fiber. The results showed that the flexural modulus doubled compared to pure PCL.

Overall, there is a lack of publications on the effects of multiple dopants on HAP formed in a fibrous form through combinations with polymers. Consequently, this work aims to investigate the physical behavior of PCL microfibers impregnated with CHAP co-doped with Mg^{2+} and SeO_3^{2-} ions at different stoichiometric contents of Mg^{2+}, with a particular focus on structural and mechanical effects potentially tunable by the dopant concentration. In addition to the physicochemical characterization, biological properties are analyzed by investigating the viability and attachment of fibroblastic cells seeded on the surface of electrospun microfibers.

Materials and methods

Synthesis of microfibrous Mg–CHAP/PCL

Calcium chloride $[CaCl_2 \cdot 2H_2O]$, diammonium phosphate $[(NH_4)_2HPO_4]$, magnesium chloride $[MgCl_2 \cdot 6H_2O]$, selenium oxide $[SeO_2]$, chloroform (99.5%), and methanol (99%) were purchased from LOBA, India, and utilized as they were received. PCL ($M_w = 80,000$) was purchased from Sigma-Aldrich. As the first step in the synthesis, a viscous PCL solution was prepared by dissolving 8 g of PCL pellets in 100 ml of the solvent composed of 66.7 ml of chloroform and 33.3 ml of methanol. Secondly, Se–CHAP (free of Mg) was prepared via a precipitation method by mixing 0.5 M of $[CaCl_2 \cdot 2H_2O]$, 0.01 M of $[SeO_2]$ and 0.29 M of $[(NH_4)_2HPO_4]$ solutions prepared by dissolving each in 50 ml of double-distilled water. The synthesis proceeded by adding the combined (P + Se) solutions into Ca solution dropwise at the rate of 1 ml/s and stirring steadily. The pH value was kept at 11.00 ± 0.05 using drops of the ammonia solution. Se–CHAP samples doped with different amounts of Mg were prepared by making 0.005, 0.01, 0.015, 0.02 and 0.025 M Mg solutions in 50 ml of double-distilled water before mixing them with the Ca solution, while keeping the ratio of (Ca + Mg)/(P + Se) = 1.67 on the basis of the following equation:

$$xMgCl_2 \cdot 5H_2O + 0.2SeO_2 \cdot 6H_2O + 5(NH_4)_2HPO_4$$
$$+ (10 - x)CaCl_2 \cdot 2H_2OMg_xCa_{(10-x)}(PO_4)_{5.8}(SeO_2)_{0.2}$$
$$(OH)_2 + 3(NH_4)(NO_3) + 6(NH_4)Cl$$

$$(1)$$

where $0.0 \leq x \leq 0.5$ with the step of 0.1.

During mixing, stirring was kept at 1200 rpm for 2 h for each sample, and then the solutions were aged for 24 h. After that, the obtained gels were washed several times with double-distilled water. Finally, a white gel was filtered and dried at 50–60 °C for 6 h. In the last step, 110 mg of each Mg–Se–CHAP sample were added to 10 ml of PCL in a sealed glass bottle to be suspended via stirring overnight. The composite samples were then introduced to a syringe pump to be processed by electrospinning. Regarding the fiber fabrication procedure, Mg–Se–CHAP/PCL microfibers were produced on a laboratory scale, using a custom-made electrospinning setup and fixed parameters for all samples. The operating parameters were as follows: the high voltage was kept at 18 ± 0.1 kV, the injection rate was 1 ml/h, the gap between the electrode and the target was 16 cm, and the syringe needle was 22φ. The flowchart of the synthesis procedure is displayed in Fig. 1.
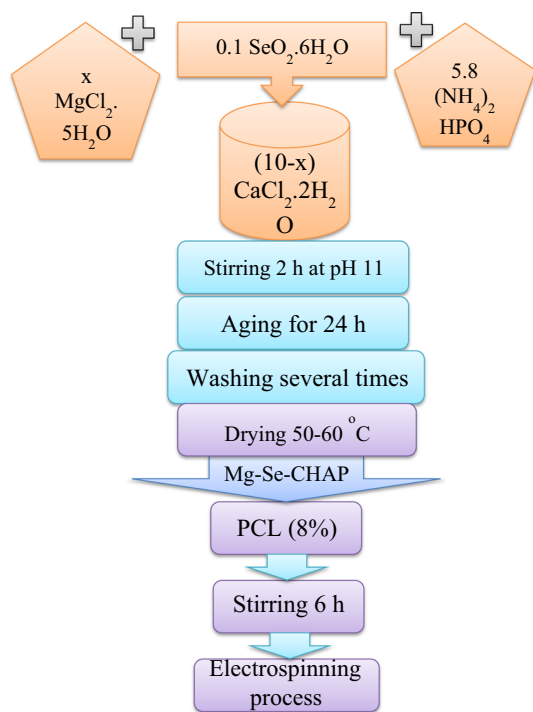

Figure 1 Block diagram of the procedure for the synthesis of Mg–Se–CHAP at different contents of the Mg^{2+} ion.

XRD measurements

X-ray diffraction (XRD) was performed on a X-ray diffractometer (analytical-x' pertpro, Cu $k_{\alpha 1}$ radiation, λ = 1.5404 Å, 45 kV, 40 mA, Netherlands). The data were collected in the range of $4° \leq 2\theta \leq 60°$ with a step size of 0.02° and the irradiation time of 0.5 s per step.

The crystallite size of HAP was calculated using Scherrer's formula [32]:

$$D = \frac{k}{\beta_{hkl} \cos}$$

$$(2)$$

where D refers to the crystallite size in nm, k represents the shape factor (0.9), λ is the wavelength of the X-rays (1.54056 Å for CuK$_\alpha$ radiation), while β_{hkl} is the full width at half maximum expressed in radians, and θ is the Bragg diffraction angle. The crystal structure of HAP was plotted using Atoms V6.3 software (Shape, Kingsport, TN).

FTIR measurements

Fourier transformed infrared (FTIR) spectra were carried out using the KBr pellet method on a FTIR spectrometer (Perkin-Elmer 2000) in the range of 4000–400 cm^{-1}.

Particle microstructure and morphology

High-resolution transmission electron microscopy (HRTEM) was utilized to examine the shape and distribution of the electrospun yield. Samples were investigated under the voltage of 200 kV on JEOL/JME model 2100. To prepare the samples for HRTEM investigation, microfibers were collected through a tube filled with distilled water, and then a copper grid was submerged into the former tube for 10 s. The surface morphology was investigated via field emission scanning electron microscope (FESEM, QUANTA-FEG250, Netherlands) under an operating voltage of 20–30 kV. The fiber diameters were measured using the ImageJ software (NIH, Bethesda, MD) [33, 34].

Roughness measurements

Micrographs of microfiber samples obtained using FESEM before treating with cells were processed with Gwyddion 2.45 software to investigate for their roughness [35]. 3D micrographs were obtained for

each sample and the resolution of the micrographs was fixed at 1450 × 900 pixels. The graphed edges were eliminated to avoid unwanted boundaries. Finally, the roughness parameters were computed using the same software in μm.

Density and porosity

Porosity ratio and real density were computed using a Quantachrome instruments analyzer (UltraPyc 1200e). The analyses were done by cutting a rectangular, (2 × 3) cm area from each sample. Then the helium gas flowed through the cell, and the averages of porosity ratio and real density were derived from three independent measurements on each sample.

The theoretical density (D_x) of Mg–Se–CHAP was computed as [4]:

$$D_x = \frac{ZM}{NV} \quad (3)$$

where M is the molecular weight of the Mg–Se–CHAP fibers, N is Avogadro's number, Z is the number of molecules per unit cell, and V is the unit cell volume. To take the contribution of PCL matrix into consideration, the total theoretical density could be formulated as [4]:

$$TD_x = AD_{x1} + BD_{x2} \quad (4)$$

where A and B represent the relative fractions of the two phases, namely Mg–Se–CHAP and PCL, respectively, equaling $A = 12.09\%$ and $B = 87.91\%$. The PCL density equaled 1.145 g/cm^3. The measured density was expressed in mass/volume units [36], while the total computed porosity was calculated as a ratio between the theoretical and measured density (ρ) as:

$$P = \left(1 - \frac{TD_x}{\rho}\right) \times 100 \quad (5)$$

Mechanical testing

The samples were prepared as rectangular strips with the dimensions of (100 × 20 × 0.1) mm. The stress/strain test was then carried out by pulling the nanofibers at the rate of 5 mm/minute up to the fracture point, as in accordance with the standard code ASTM D882.

HFB4 attachment onto the microfibers

FESEM was used to observe the growth behavior of HFB4 cells seeded on the microfibers. For this purpose, each sample was cropped into two pieces of 0.5 × 0.5 cm, which were then exposed to a UV lamp in 12-well plates for 30 min for sterilization. Then 1.5 ml of HFB4 cells (5 × 10^5 cells) was added into each well. Lastly, the plate was covered and incubated at 37 °C for three days. After this time, the fibers were washed with phosphate buffer saline (PBS). To keep the cells fixed on the nanofiber surface, the scaffolds were submerged in a glutaraldehyde solution (4% concentration) for 1.0 h. They were then dehydrated in air for 15 min. Finally, they were sputtered with gold for 2 min to be ready for FESEM imaging.

In vitro cell viability tests

The human osteoblast cell line, HFB4, was cultured in Dulbecco's modified Eagles medium (DMEM, Gibpco) at 37 °C and 5% CO$_2$ to investigate the viability of cells seeded onto the microfibers. Cells seeded at the density of 5 × 10^3 cells/cm^2 were cultured on the fibers in 12-well plates. After 3 days of incubation at 37 °C, the medium was removed and MTT (3-(4,5-dimethylthiazol-2-yl)-2,5-diphenyltetrazolium bromide) injected into each well, after which the cell viability was detected via an optical analyzer.

Cell viability could be described as the percentage of viable cells relative to the total cell number as [37]:

$$\text{Viability}(\%) = \frac{\text{Mean optical density of test samples}}{\text{Mean optical density of the control}} \times 100$$

Results and discussion

Structural analysis

X-ray diffraction (XRD) patterns of pure Mg–Se–CHAP and of Mg–Se–CHAP/PCL composite microfibers at different contents of Mg^{2+} in Mg–Se–CHAP are shown in Fig. 2. They illustrate that the microfiber samples were biphasic, with the diffraction peaks of a higher intensity ($2\theta = 21.329°$, $23.678°$ and $25.72°$)
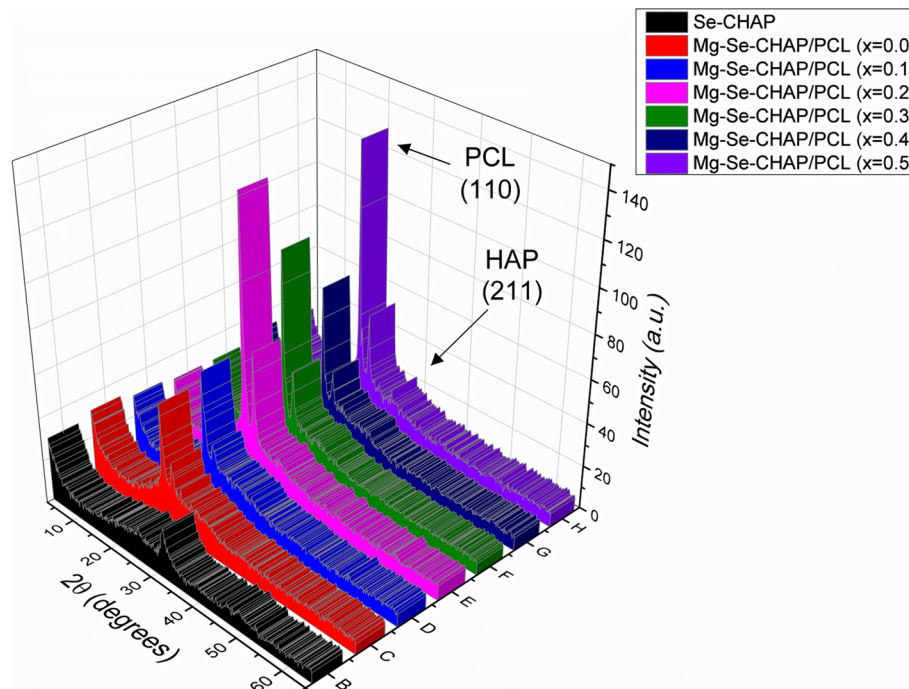
Figure 2 XRD patterns of Se–CHAP and of $Mg_xCa_{(10-x)}(PO_4)_{5.8}(SeO_2)_{0.2}(OH)_2]$/PCL composite scaffolds at different contents of the Mg^{2+} ion in the Mg–Se–CHAP phase.
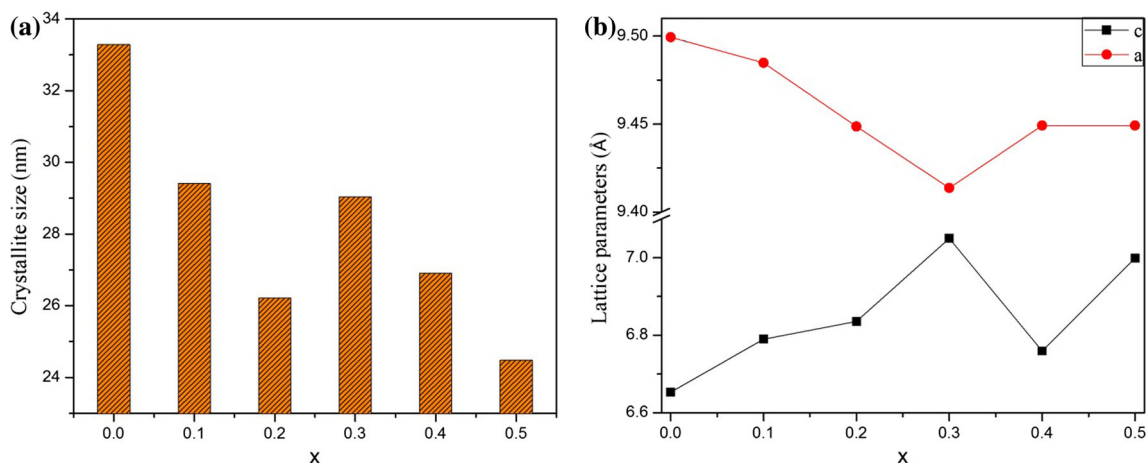

Figure 3 Variation of the crystallite size and lattice parameters as a function of the Mg^{2+} ion content in the Mg–Se–CHAP phase of Mg–Se–CHAP/PCL fibers: **a** crystallite size and **b** lattice parameters a and c.

attributed to PCL and the peaks of a lower intensity (2θ = 31.63°, 32.42° and 33.25°) assigned to HAP, which was indexed as a hexagonal structure with the $P6_3/m$ space group per ICDD card No. 01-073-0293. No ternary phases were observed as originating from Mg^{2+} or Se^{4+} ions, which means that these ions were trapped successfully into the HAP lattice.

The average Mg–Se–CHAP crystallite size values calculated from the Scherrer equation are represented in Fig. 3a. The chart illustrates that the crystallite size

has a general tendency to decrease as the Mg^{2+} content in the composite rises, dropping from 33.3 nm at $x = 0.0$ to 24.5 nm at $x = 0.5$. Figure 3b shows the dependence of the lattice parameters on the Mg^{2+} content in Mg–Se–CHAP. This dependence is complex and, as seen in Fig. 3b, the lattice parameter a tends to decrease dramatically in the $x = 0.0$–0.3 range, after which it begins to rise slightly. The lowest value achieved at $x = 0.3$ was 9.414 Å, which indicates a deviation of 0.9% compared to the

undoped sample ($x = 0.0$). On the other hand, the lattice parameter c shows the opposite trend, as it increases in the $x = 0.0$–0.3 range, after which it drops sharply between $x = 0.3$ and $x = 0.4$. The highest value achieved at $x = 0.3$ deviated by around 5.9% relative to $x = 0.0$. In this relatively low range of Mg^{2+} concentrations ($x = 0.0$–0.3), the trend in the change of the lattice parameters a and c with the Mg^{2+} content is in agreement with the results of the study by Safarzadeh et al. [38]. Namely, this group studied the structural influence of small amounts of ionic dopants in CHAP and found out that the c/a ratio increases with an increase in the Mg^{2+} concentration in CHAP.

In HAP structure, there are two different sites for Ca^{2+} ions: columnar Ca(1) and hexagonal Ca(2) (Fig. 4) [39]. In our case, HAP undergoes spontaneous substitution with carbonate ions entering the compound as CO_2 from the ambient atmosphere. In addition to this, the samples were systematically doped with SeO_3^{2-} and Mg^{2+} ions in varying amounts. Selenite is expected to predominantly occupy phosphate sites, while carbonate competes with selenite ions for the replacement of the phosphate positions (B-type of CHAP) in addition to replacing hydroxyl sites to a minor degree (A-type CHAP). Consequently, the situation has a plethora of prospective scenarios, and to analyze it, a few postulates could be proposed. The first assumption is
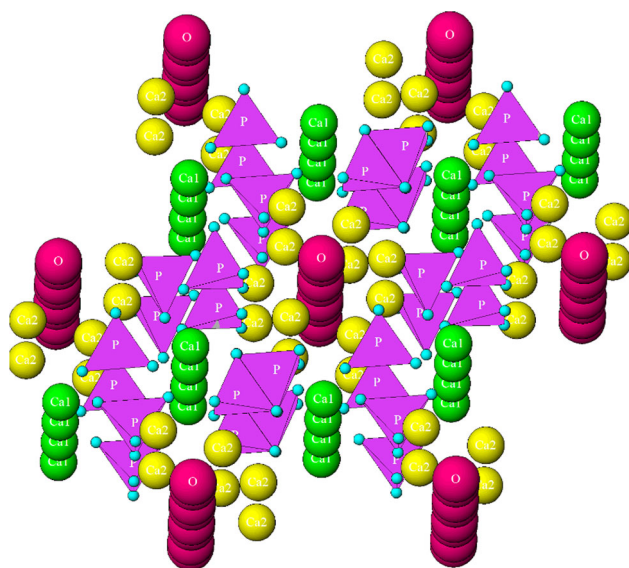

Figure 4 Hexagonal crystal structure of HAP showing columnar, Ca1 calcium ions in green, hexagonal, Ca2 calcium ions in yellow, hydroxyl groups in magenta, and phosphate tetrahedral in purple.

that the phosphate sites are expected to be replaced by both carbonate and selenite ions. Although it is not clear where the carbonate would get accommodated exactly, the lattice parameters could be a useful tool to approximate its location. Due to its triangular shape, the carbonate exchange could be accomplished with the resulting contraction of the unit cell a-axis and expansion of the c-axis as well as the probable formation of a lattice vacancy to preserve the charge neutrality. The release of a Ca^{2+} and OH^- ion pair to compensate for the charge imbalance and the consequential formation of a Schottky defect is another possible scenario.

Due to the charge difference between selenite (-2) and phosphate (-3), the oxygen oxyanion tends to be redistributed around the central ion, as the columnar shape of the tetrahedral phosphate cedes place to the flat trigonal pyramidal shape of the selenite [28]. This may cause c-axis contraction and may further influence the morphology and particle size of the obtained composition, not to mention the properties and potential applications. Wei et al. studied the effect of Sr^{2+} content variation in Se–HAP where the selenite content was kept constant at 1.4 mM. The results indicated that both a-axis and c-axis expanded with the Sr^{2+} content, with the former starting off from 9.373 Å at the zero content of Sr^{2+} and reaching 9.438 Å at Sr/(Ca + Sr) = 0.2 [3]. In contrast, Wei et al. [29] investigated the influence of the selenite dopant in HAP and found out that a-axis increased and c-axis decreased with the addition of selenite from zero to Se/P = 0.3. The latter trend was confirmed by Sun et al. [28].

Concerning the Ca^{2+} ion exchange, it was reported that Ca(2) volume is larger than Ca(1) [5]. Also, the ionic charge and the related bond strength are the main factors that determine which ionic exchange scenario will apply. Mg^{2+} ion has four coordination states, corresponding to the coordination numbers (CNs) of 4, 5, 6 and 8. In contrast, the CNs of Ca(1) and Ca(2) are 9 and 7, respectively. It was noticed that the c/a ratio increases with x, which indicates that the expansion is mainly in the direction of the c-axis. Together with the fact that the ionic radius of Mg^{2+} in the coordination state defined by CN = 8 and the ionic radius of Ca^{2+} in the coordination state defined by CN = 7 are 0.89 and 1.18 Å, respectively [40], this may indicate that Mg^{2+} ions preferentially substitute Ca(2) sites. In an earlier study, Lala et al. [41] investigated the structural behavior of CHAP

substituted with Mg^{2+} ions and concluded that Mg^{2+} preferentially accommodates itself at Ca(2) sites. The reversal of the lattice change trend at $x > 0.03$, however, suggests that at higher weight contents, Mg^{2+} may change its lattice accommodation preference from Ca(2) to Ca(1).

FTIR spectroscopy

FTIR spectra of Mg–Se–CHAP/PCL composite microfibers at different contents of Mg^{2+} in Mg–Se–CHAP are displayed in Fig. 5. The following absorption bands related to CHAP were discernible in the spectra: 960.4 cm^{-1} and 1043.3 cm^{-1} represent (v_1) and (v_3) stretches of PO_4^{3-}, while (v_4) bend of PO_4^{3-} was displayed as a doublet at 568.9 cm^{-1} and 599.8 cm^{-1} and (v_2) bend of PO_4^{3-} as a singlet at circa 460 cm^{-1}. O–Se–O asymmetric bond stretch (v_3) from the selenite group was detected at 730.9 cm^{-1} [1, 32, 42, 43]. Regarding the carbonate group, the bands peaking at 1416.5 cm^{-1} and 1463.7 cm^{-1} are associable with the (v_3) vibration in B-type CHAP
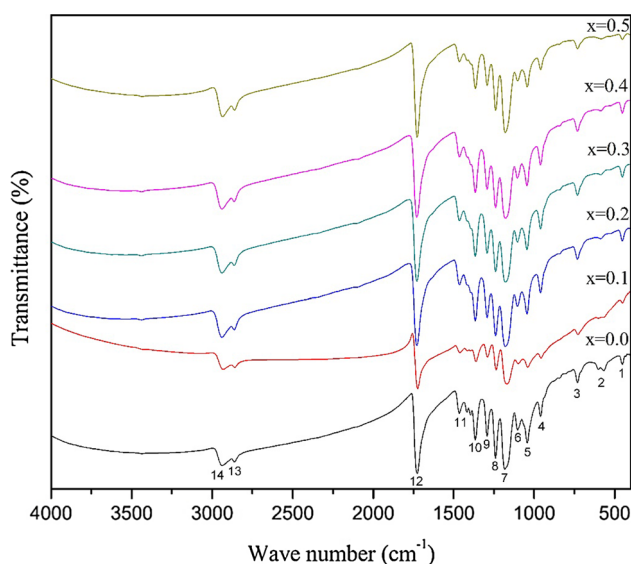

Figure 5 FTIR spectra of the Mg–Se–CHAP/PCL composite at different contents of the Mg^{2+} ion in Mg–Se–CHAP ($x = 0.0$–0.5). Band assignments are as follows: 1—$v_2(PO_4^{3-})$ from Mg–Se–CHAP; 2—$v_4(PO_4^{3-})$ from Mg–Se–CHAP; 3—$v_3(SeO_3^{2-})$ from Mg–Se–CHAP; 4—$v_1(PO_4^{3-})$ from Mg–Se–CHAP; 5—$v_3(PO_4^{3-})$ from Mg–Se–CHAP; 6—$v_1(CO_3^{2-})$ from Mg–Se–CHAP; 7, 8, 9—v_3(C–O/C–C) from PCL; 10—v_1(C–O–C) from PCL; 11—$v_3(CO_3^{2-})$ from Mg–Se–CHAP; 12—v_1(C=O) from PCL; 13—v_1(H–C–H) from PCL; 14—v_3(H–C–H) from PCL.

[44–46]. In addition, 1180.2, 1240 and 1292.1 cm^{-1} bands could be assigned to the C–O–C group, namely the v_3 asymmetric stretch of C–O and C–C, respectively, originating from semi-crystalline PCL [42]. Also, the 1726.9 cm^{-1} band originates from the C=O stretch, while the characteristic bands at 2861.8 and 2936.1 cm^{-1} refer to the symmetric (v_1) and asymmetric (v_3) stretching modes of CH_2, respectively [42]. Therefore, all the characteristic bands of CHAP and PCL, as reported in Table 1, have appeared in the spectra of Mg–Se–CHAP/PCL microfibers, indicating the successful blending of CHAP into the fibrous PCL matrix. Moreover, a closer look at the v_3(C–O) stretching mode in PCL shows that this vibration mode exhibits a downshift as Mg^{2+} is introduced into Se–CHAP (Fig. 6). This lowering of the vibration energy is characteristic for stretching modes undergoing interaction with another phase, in this case, Mg–Se–CHAP. The effect was most intense upon the first introduction of Mg^{2+} to Se–CHAP, at $x = 0.1$, and normalized at higher Mg^{2+} contents while preserving a steadily lower vibrational energy state compared to undoped Mg–Se–CHAP incorporated in PCL.

Morphological behavior

Morphological properties of electrospun polymeric fibers are known to depend on synthesis parameters such as viscosity and solvent polarity, which could all be affected by the size and concentration of particulate additives, in this case, Mg–Se–CHAP. To minimize these effects on the material properties, the particle content in the polymer was kept constant and only the concentration of the Mg^{2+} dopant inside the particles was varied. Therefore, notwithstanding that the variation of Mg^{2+} concentration inside the particles is bound to affect specific Mg–Se–CHAP particle properties, which may, in turn, affect the properties of the polymer–solvent interaction and thus the properties of the produced composite material, the setup of this study allowed us to assess the effect of solely the variation in Mg^{2+} concentration inside the Mg–Se–CHAP particles.

Figure 7a–f shows the surface morphology of $Mg_xCa_{(10-x)}(PO_4)_{5.8}(SeO_2)_{0.2}(OH)_2$]/PCL composite fibers at different contents of the Mg^{2+} ion in the $0.0 \leq x \leq 0.5$ range. Figure 7a, b shows the surface image of the $x = 0.0$ composition, where it is seen that the fibers adopt a preferred orientation, almost like a

Table 1 Characteristic FTIR bands of Mg–Se–CHAP/PCL fibers at different contents of the Mg^{2+} ion

| $x = 0.0$	$x = 0.1$	$x = 0.2$	$x = 0.3$	$x = 0.4$	$x = 0.5$	Assignment	References
453.2	452.2	452.2	452.2	453.2	452.2	(v_4) of O–P–O	[51]
568.9	–	587.2	585.3	568.9	584.3	(v_4) of PO_4^{3-}	[52–54]
599.8	601.7	–	–	598.8	–	(v_4) of PO_4^{3-}	[37, 52]
730.9	728.0	731.9	731.9	731.9	730.9	(v_3) of Se–O	[45]
960.4	957.5	960.4	961.3	960.4	960.4	(v_1) of PO_4^{3-}	[30, 55]
1043.3	1039.4	1045.2	1046.2	1044.3	1044.3	(v_3) of PO_4^{3-}	[56]
1101.2	1099.2	1104.1	1104.1	1102.1	1103.1	P–O stretch	[57]
1180.2	1169.6	1180.2	1178.3	1180.2	1180.2	C–O–C	[58]
1240	1236.2	1240.0	1240.0	1240.0	1239.0	C–O–C	[55, 58]
1292.1	1290.1	1293.0	1293.0	1293.0	1292.1	C–O and C–C	[30, 58]
1416.5	–	–	–	–	1416.5	(v_3) of CO_3^{3-}	[27, 29]
1463.7	1460.8	1464.7	1463.7	1463.7	1463.7	(v_3) of CO_3^{3-}	[27, 57]
1726.9	1723.1	1728.9	1729.8	1728.9	1726.9	C=O	[30, 58]
2861.8	2860.9	2863.8	2864.7	2862.8	2860.9	C–H stretch	[30, 58]
2936.1	2931.3	2939.0	2940.9	2939.0	2935.1	C–H stretch	[58]
3433.6	–	3438.5	3440.4	3435.6	3433.6	O–H stretch	[35, 53, 55]
–	–	3536.8	–	–	–		
–	–	–	3630.3	–	–		
–	–	–	3756.7	–	–		
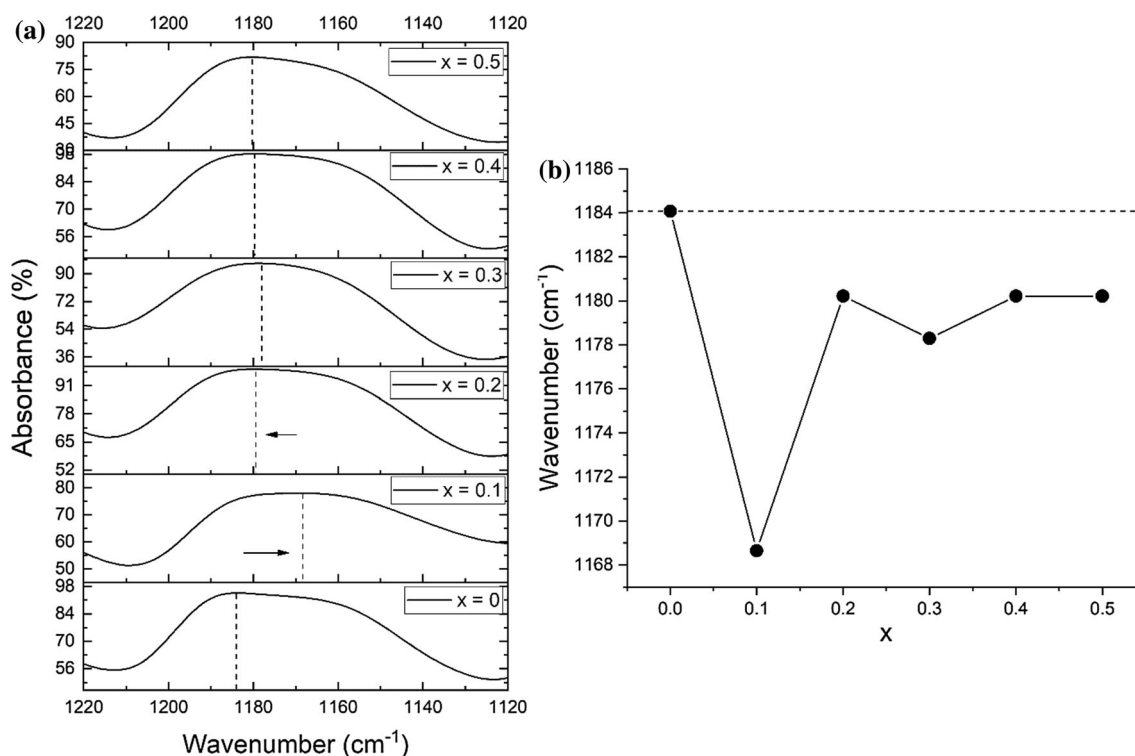
Figure 6 FTIR spectra of the Mg–Se–CHAP/PCL composite at different contents of the Mg^{2+} ion in Mg–Se–CHAP ($x = 0.0$–0.5) focusing on the v_3(C–O) stretching mode in PCL in the 1220–1120 cm^{-1} range (**a**). Shift of the v_3(C–O) stretching mode (#7 in Fig. 5) as a function of the Mg^{2+} content in Mg–Se–CHAP ($x = 0.0$–0.5) (**b**). Dashed line in **b** represents the vibration maximum in the Se–CHAP/PCL composite.
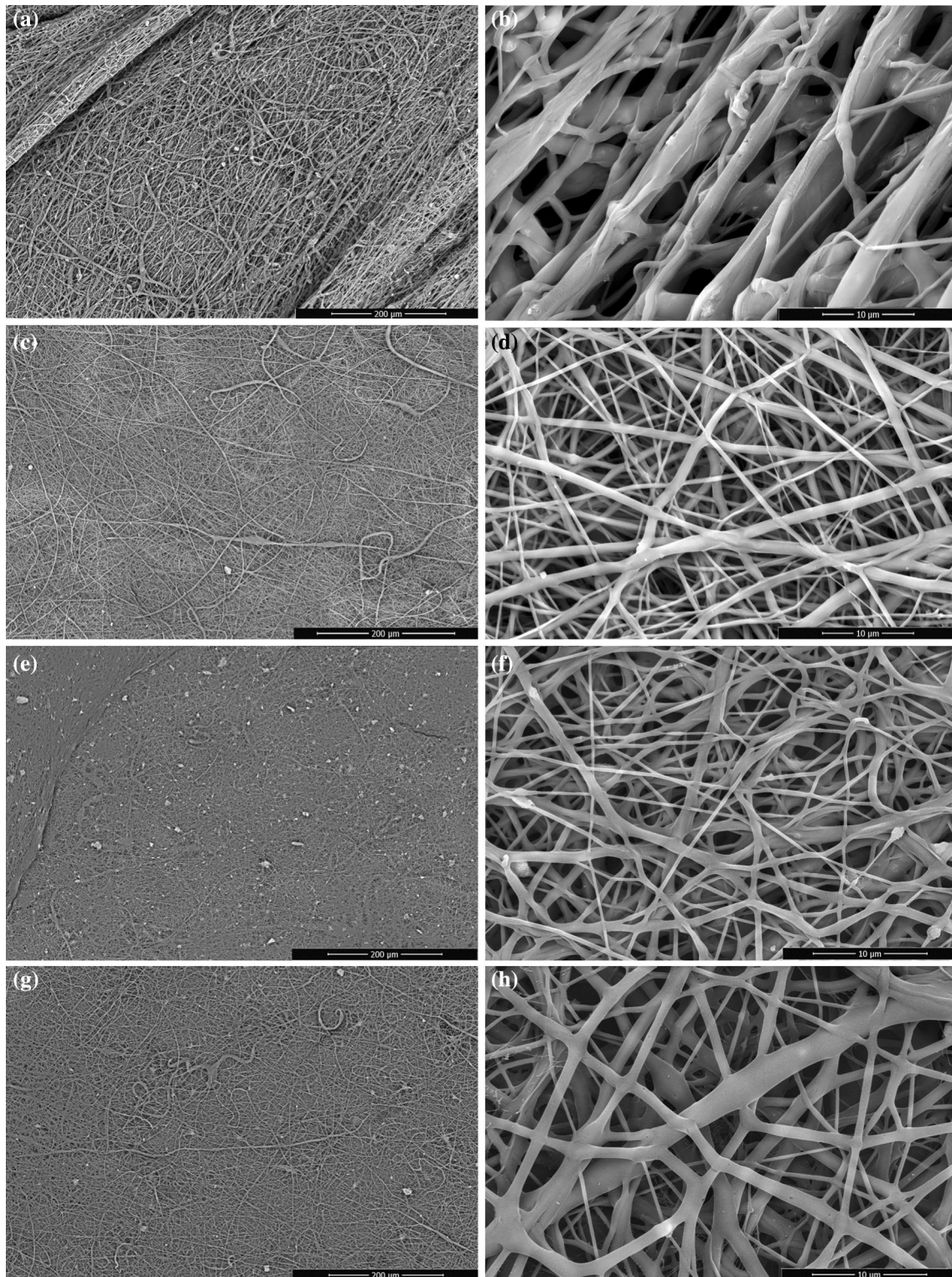
Figure 7 a–h FESEM micrographs of $Mg_xCa_{(10-x)}(PO_4)_{5.8}$ $(SeO_2)_{0.2}(OH)_2]$/PCL at different contents of the Mg^{2+} ion in the Mg–Se–CHAP phase: **a, b** $x = 0.0$, **c, d** $x = 0.2$, **e, f** $x = 0.4$, **g, h** $x = 0.5$. **i** Histograms representing the average diameter of the fibers for different x.
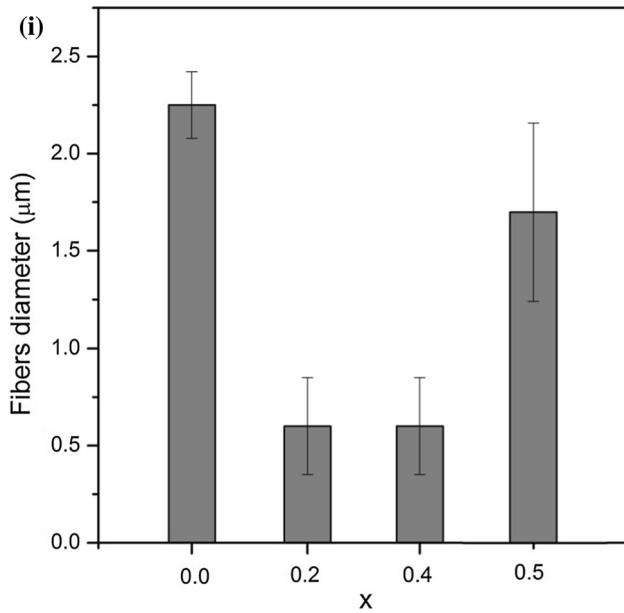
Figure 7 continued.

texture, with the diameter of the main fibers being 2–2.5 μm. However, these main fibers appear to be cross-linked transversely via thinner nanofibers whose diameter is around 0.5 μm. Here it should be noted that no consistent changes in full width at half maximum of signature PCL bands in FTIR spectra or in integrated peak intensities entailed this formation of links between individual fibers, suggesting that this bridging effect may be primarily physical and morphological in nature rather than chemical. Nodes could be observed on the surface of the main fibers, with distances of around 20 μm, signifying the finite roughness of the fibers. In addition, these electrospun fibers exhibit fine porosity, which is crucial for the transport of nutrients and the formation of blood vessels after the implantation within a hard or soft tissue. Figure 7c, d refers to the $x = 0.2$ composition and shows a more significant variation in the fiber diameter distribution compared to the $x = 0.0$ composition. A wide range of randomly oriented nanofibers appeared with a diameter in the range of 0.25–1.0 μm. Moreover, nodes with the distances of 17 μm could be found along the length of the microfibers, whereas the pores had a more regular distribution than the $x = 0.0$ composition. Figure 7e, f displays the $x = 0.4$ composition, which looks like a complicated network with fiber diameters in the range of 0.25–1.0 μm. The fibers seem to be oblique rather than completely cylindrical and the nodes on the fibers appeared even shorter than $x = 0.0$ and

$x = 0.2$ compositions, around 5 μm in length, which may explain the higher degree of branching that leads to the complex nature of this composition. Finally, Fig. 7g, h represents the $x = 0.5$ composition, where two types of fibers are discernible depending on their diameter: the main ones with the diameter of 1–2.4 μm and the thinner ones with 0.4 μm in diameter. In addition to this, the fibers are linked with an ultrafine nanofiber network, like spiderweb, with diameters not exceeding 90 nm. The observed nodes are randomly distributed along the fibers with distances ranging from 7 to 20 μm. Although this ultrafine, nanosized spiderweb may improve the fracture toughness of this composition, it also reduces the porosity, thus potentially limiting the cell proliferation, transport of nutrients and angiogenesis.

Consequently, with an increase in the amount of Mg^{2+} in the Mg–Se–CHAP component of the fibrous PCL composite, the distribution of the fiber dimensions broadens, while the interaction between the fibers tightens, which will reflect strongly on the mechanical and biological behavior of the material. The key properties of interest here, specifically the mechanical and biological properties, including the fracture strength and stability in a biological environment, are therefore expected to change as a function of the concentration of the Mg^{2+} dopant. The primary purpose of producing HAP in a fibrous form is to enhance its fracture toughness so as to resist the crack formation and/or prevent its propagation. Shortly, we will show that the concentration of the Mg^{2+} dopant confined solely to the ceramic phase indeed improves this toughness. Still, one downside of this improvement via a higher degree of bridge formation between individual fibers and a broader fiber diameter distribution is that the porosity may be lower than the ideal for facilitating the vascularization process. Namely, the morphological studies have shown that the volume of pores gets significantly reduced with an increase in the Mg^{2+} ion content. Therefore, the compensation between mechanical and biological requirements are needed to obtain the optimum conditions to be utilized for the desired application.

Figure 8a–d shows the surface roughness as a function of the variation in the Mg^{2+} content in the ceramic phase of the fibrous Mg–Se–CHAP/PCL composite. The roughness average (R_a) started from 34 nm at $x = 0.0$, then it reached 84 nm at $x = 0.2$, but then plunged down to 44 nm at $x = 0.5$. The root-
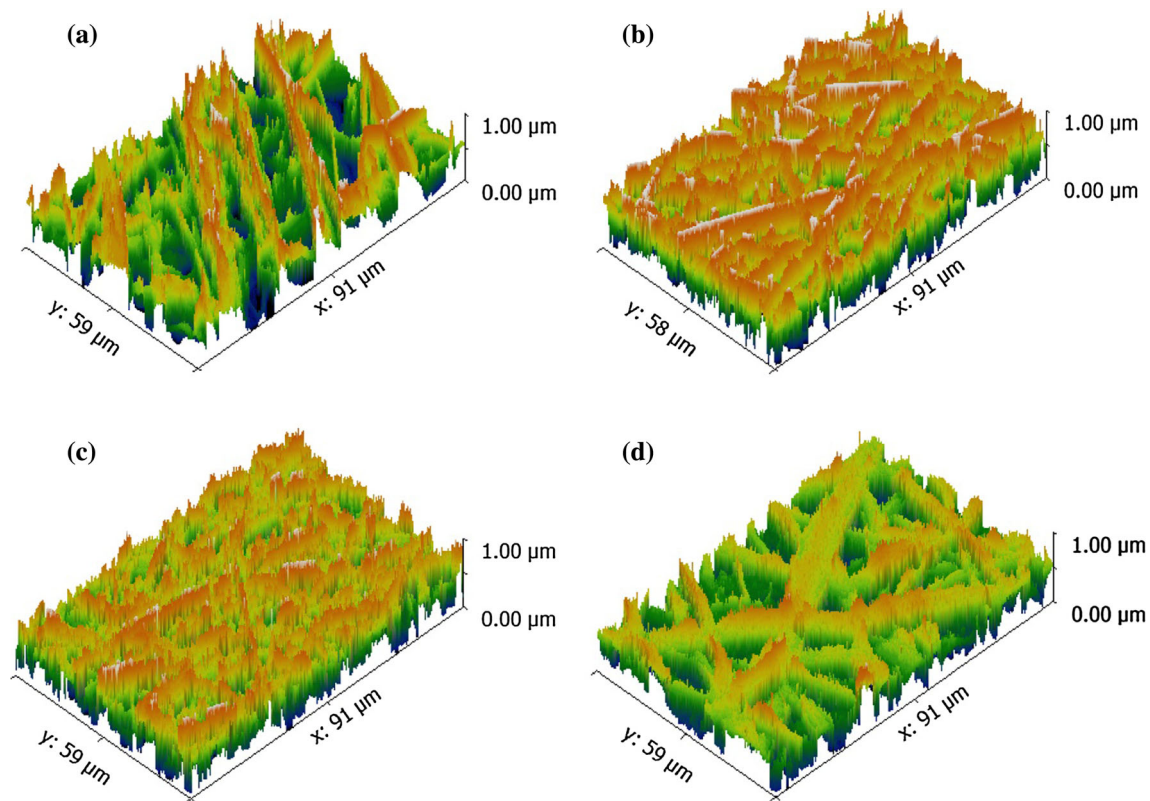
Figure 8 a–d Surface roughness micrographs of $\{Mg_xCa_{(10-x)}(PO_4)_{5.8}(SeO_2)_{0.2}(OH)_2]/PCL\}$ at different contents of the Mg^{2+} ion in the Mg–Se–CHAP phase; **a** $x = 0.0$, **b** $x = 0.2$, **c** $x = 0.4$, **d** $x = 0.5$.

Table 2 Surface roughness parameters of Mg–Se–CHAP/PCL fibers at different contents of the Mg^{2+} ion, including roughness average [R_a], root-mean-square roughness [R_q], maximum height of the roughness [R_t], maximum roughness valley depth [R_v], maximum roughness peak height [R_p], average maximum height of the roughness [R_{tm}], average maximum roughness valley depth [R_{vm}], average maximum roughness peak height [R_{pm}] and root-mean-square waviness [W_q]

x	R_a (nm)	R_q (nm)	R_t (nm)	R_v (nm)	R_p (nm)	R_{tm} (nm)	R_{vm} (nm)	R_{pm} (nm)	W_q (nm)
0.0	34	48	417	197	220	312	142	170	238
0.2	84	112	808	424	384	632	309	323	226
0.4	66	87	655	297	358	547	258	289	175
0.5	44	64	627	340	287	413	205	208	176

mean-square roughness exhibited the same trend, with a maximum value of 112 nm at $x = 0.2$ and a minimum value of 48 nm at $x = 0.0$. On the other hand, the root-mean-square waviness (W_q) dropped dramatically with the Mg^{2+} content; it peaked at 238 nm for $x = 0.0$ and exhibited minima at 175 and 176 nm for $x = 0.4$ and $x = 0.5$, respectively. As seen from Table 2, the surface roughness varied with the amount of Mg^{2+} ions incorporated into Se–CHAP lattice, despite the fact the variation did not respond linearly to an increase in the Mg^{2+} content. Surface

roughness is one of the most significant parameters defining the interaction with the host environment. Specifically, rough surfaces are more active than the smooth ones and many cell types, including fibroblastic cells, proliferate or differentiate markedly better on rough surfaces than on the smooth ones [47]. The origins of these changes in roughness may be sought in the inherently disordering effects exerted by the external dopants on the structure of HAP. Ionic exchanges and interstitial ions in addition to the irregular distribution of charges cause crystal

distortions and lead to the formation of lattice defects [48]. These defects possess a higher energy than the regular, non-defective sites and chemical interaction is preferred at these defected sites than on the regular ones. Connecting the surface roughness and fiber interconnectedness, it can be hypothesized that more defects would induce the bridge formation not only between individual composite fibers, but also between the implant material and the host tissue, which would accelerate the healing process. In addition to this, this higher surface energy has a greater propensity to absorb dislocations and mitigate crack propagation than its lower energy counterpart. Because the surface roughness does not change linearly with the Mg^{2+} content, the dopant content must be carefully optimized and compensations must be made between multiple properties of interest.

Porosity

Table 3 shows that the theoretical density for the investigated samples decreases with an increase in the Mg^{2+} concentration in the Mg–Se–CHAP phase. Thus, the measured density was 0.1299 g/cm^3 for $x = 0.0$ and it increased by more than twofold, up to 0.2858 g/cm^3 for $x = 0.4$, after which it decreased at higher Mg^{2+} contents. Regarding the porosity ratio, the highest value was achieved at $x = 0.0$, equaling 90.66%, while the lowest one was achieved at $x = 0.3$, equaling 79.17%. These comparatively high values of porosity support the transport of oxygen and nutrients through the material and may be crucial for facilitating the healing process, albeit having a negative impact on the mechanical properties. Sattary et al. [42] studied the physical and chemical behavior of nanosized HAP incorporation in PCL/gelatin scaffolds produced via electrospinning and found out that the porosity ratio of both pure PCL and PCL/gelatin/HAP was between 80 and 81%, while Shkarina measured the porosity ratio of electrospun

PCL containing Si-HAP to be in the same range: 78.36 ± 3.35% [49]. In conclusion of the morphological analysis part, it can be said that, as in agreement with previous studies [50], there are reasons to suspect that PCL nanocomposites may be very good candidates for scaffolds for the reconstruction of bone defects and fractures.

Cell viability

To investigate the cell response to the material, the HFB4 cells were exposed to the fibers and their viabilities after 72 h of incubation were indistinguishable from the controls, equaling 97.3 ± 3.2% and 95.81 ± 4.3% for $x = 0.0$ and $x = 0.5$ compositions, respectively, as it is shown in Fig. 9. The viability of cells is the first and foremost factor determining the usability of the composite for clinical application. The addition of Mg^{2+} to Se–CHAP incorporated within electrospun PCL fibers had no negative impact on the cell mortality, which may suggest that it can be further investigated for bone scaffold applications.

Cell adhesion and spreading

Results of the assays investigating the HFB4 cell growth, adhesion, and proliferation on Mg–Se–CHAP/PCL fibrous scaffolds are shown in Fig. 10a–l. Figure 10a, b illustrates that cells did not only grow on the surface of the electrospun material at $x = 0.0$, but they also proliferated into the subsurface pores, which gives their cell spreading an ever more positive dimension. Increasing the content of Mg^{2+} in Mg–Se–CHAP to $x = 0.1$, as it is shown in Fig. 10c, d, produced a minor change in cell adhesion, but the higher magnification image (Fig. 10d) indicates that the cell spreading was more intense than at $x = 0.0$ and suggests that the addition of Mg^{2+} to the Mg–Se–CHAP phase, even though the latter may not be as prominent on the fiber surface as the molecules of the

Table 3 The theoretical density (TD_x), the measured density (ρ), and the porosity ratio of Mg–Se–CHAP/PCL fibers at different concentrations of the Mg^{2+} ion

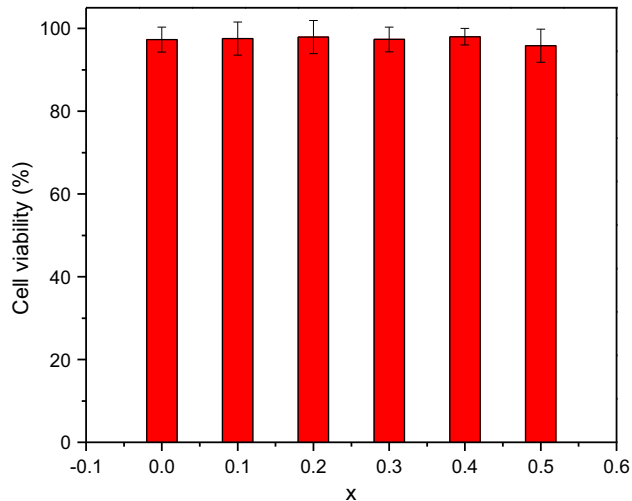| x	D_x (Mg–Se–CHAP)	TD_x (g/cm^3)	ρ (g/cm^3)	Porosity (%)
0.0	3.17	1.390	0.1299	90.66
0.1	3.11	1.383	0.1732	87.47
0.2	3.11	1.382	0.2704	80.43
0.3	3.03	1.372	0.2858	79.17
0.4	3.12	1.384	0.2507	81.89
0.5	3.01	1.370	0.1701	87.59

Figure 9 Cell viability of Mg–Se–CHAP/PCL fibers at different contents of the Mg^{2+} ion in the Mg–Se–CHAP phase.

polymeric phase, substantially improves the cell adhesion properties of the material.

Figure 10e, f shows a further improvement as the Mg^{2+} content is increased up to $x = 0.2$. Namely, the cells have now grown at a higher density and a higher proliferation rate than on the compositions with the lower Mg^{2+} content, and they also seem to fill the pores of the matrix. This implies that there is a considerable change at $x = 0.2$ compared to the lower Mg^{2+} contents, which is matching well with the results of the roughness analysis, where this particular polymeric matrix ($x = 0.2$) was shown to possess the roughest surface of them all. This link between the surface roughness and the cell growth hints at the significant influence of surface defects, which are markedly affected by the dopant content. The relationship between the dopant content and biocompatibility could be, thus, described with a simple causative link as follows: the dopant concentration → defects → surface roughness → high energy → high chemical activity → bond formation (interaction) → adhesion → biocompatibility.

Figure 10g, h shows the cell attachment on the surface of Mg–Se–CHAP/PCL fibrous scaffolds at $x = 0.3$, with the pores appearing filled with cells, while Fig. 10i, j shows the same effect of $x = 0.4$. A thick layer of grown cells is observed on the fiber surface, indicating the potential for deeper cellular penetration on the polymeric scaffold. Finally, Fig. 10k, l shows the spreading of the cellular units on the surface of Mg–Se–CHAP/PCL at $x = 0.5$. These analyses clearly indicate that there is a

considerable effect exhibited by the Mg^{2+} content on cells attaching onto the surface of the composite material. The proliferation of HFB4 cells has been impacted positively by an increase in the Mg^{2+} content, both at lower doses (Fig. 10a–f at $x = 0.0$–0.3) and at higher ones (Fig. 10i–l at $x = 0.4$–0.5). This agrees well with the previous studies that indicated that Mg^{2+} has a positive effect on inducing fibroblastic and osteoclastic processes in the newly formed bone [5, 46].

Mechanical behavior

The dependency of tensile stress–strain behavior on the content of the Mg^{2+} dopant in the Mg–Se–CHAP component of Mg–Se–CHAP/PCL scaffolds is shown in Fig. 11a. It could be noticed that the maximal tensile strength grows exponentially from $x = 0.0$ to $x = 0.2$, at which point it reaches its highest value of 16.90 MPa, fourteen times higher than the 1.21 MPa measured for the $x = 0.0$ composition.

Bone is the most critical load-supporting tissue in the body. Therefore, one of its basic characteristics is its high toughness, which is needed to prevent fracture during movement and is proportional to the absorbed energy prior to the fracture. Pure ceramics, including HAP, are brittle and are thus not ideal for utilization in load-bearing applications as pure phases. For this reason, HAP/polymer composites are being designed as materials that enhance the toughness of HAP. As it can be seen in Fig. 11b, toughness does get improved not only with the combination of HAP with PCL, but also with the incorporation of Mg^{2+} into HAP lattice. The highest value of 6.79 MJ/m^3 was achieved at $x = 0.2$ and the lowest value of 0.79 MJ/m^3 was achieved at $x = 0.0$. Interestingly, as it is seen in Fig. 11b, c, both tensile strength and toughness peak at $x = 0.2$, which is the composition lying close to the deflection point for a number of crystallographic parameters describing the Mg–Se–CHAP lattice. It was also the composition with the highest roughness and the most proliferative cell spread. These results demonstrate that doping Se–CHAP with Mg^{2+} produces internal crystallographic changes that are reflected in the overall interaction between the HAP phase and the polymeric phase, affecting in turn both the mechanical properties, the microstructure and the cell response. Therefore, it is shown from various standpoints that the substitution of ions in the lattice of HAP may enhance structural,
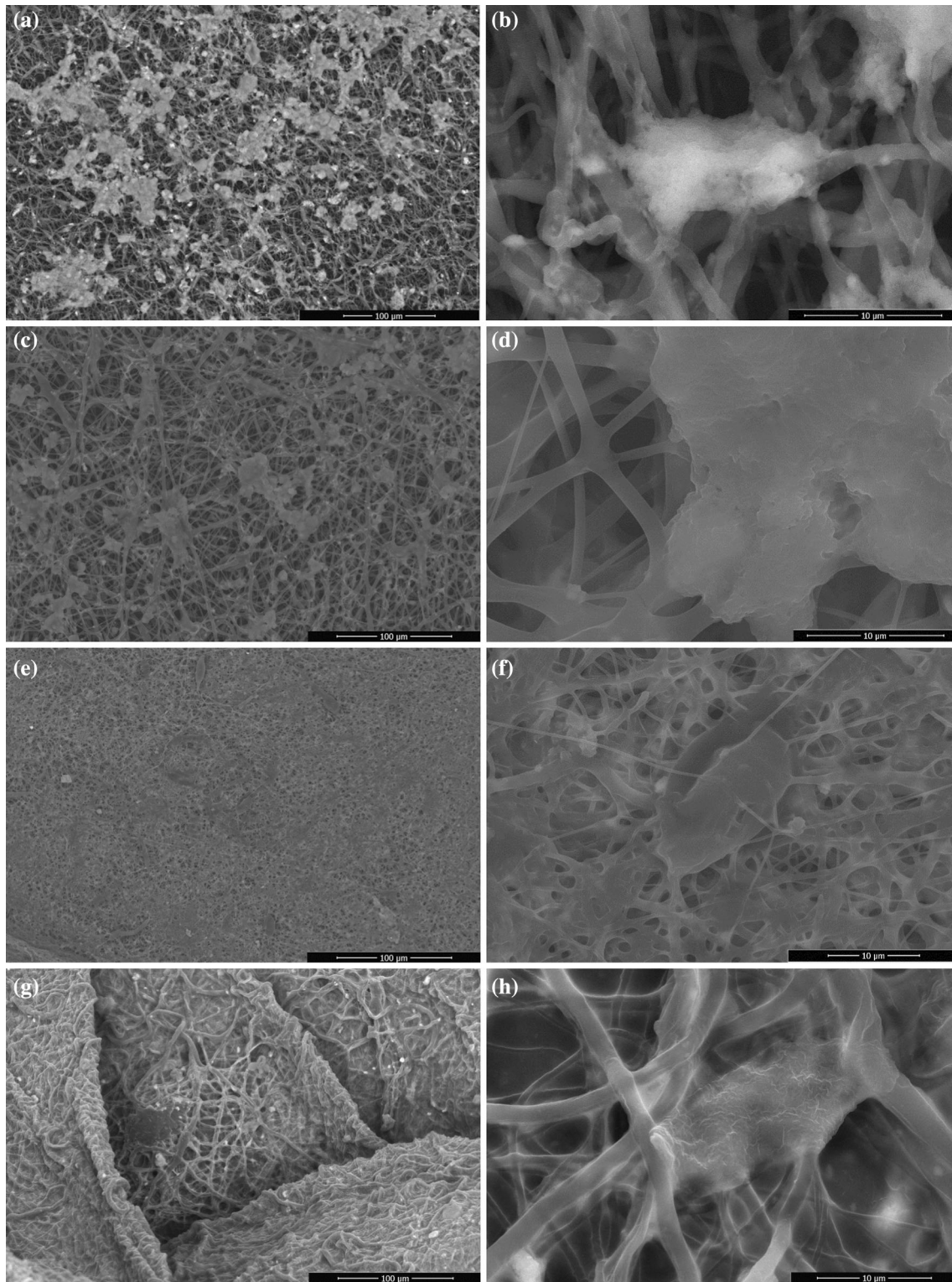
Figure 10 **a–l** HFB4 cell growth on {Mg$_x$Ca$_{(10-x)}$(PO$_4$)$_{5.8}$(SeO$_2$)$_{0.2}$(OH)$_2$]/PCL} scaffolds at different contents of the Mg ion in the Mg–Se–CHAP phase after 3 days of incubation; **a**, **b** $x = 0.0$, **c**, **d** $x = 0.1$, **e**, **f** $x = 0.2$, **g**, **h** $x = 0.3$, **i**, **j** $x = 0.4$ and **k**, **l** $x = 0.5$.
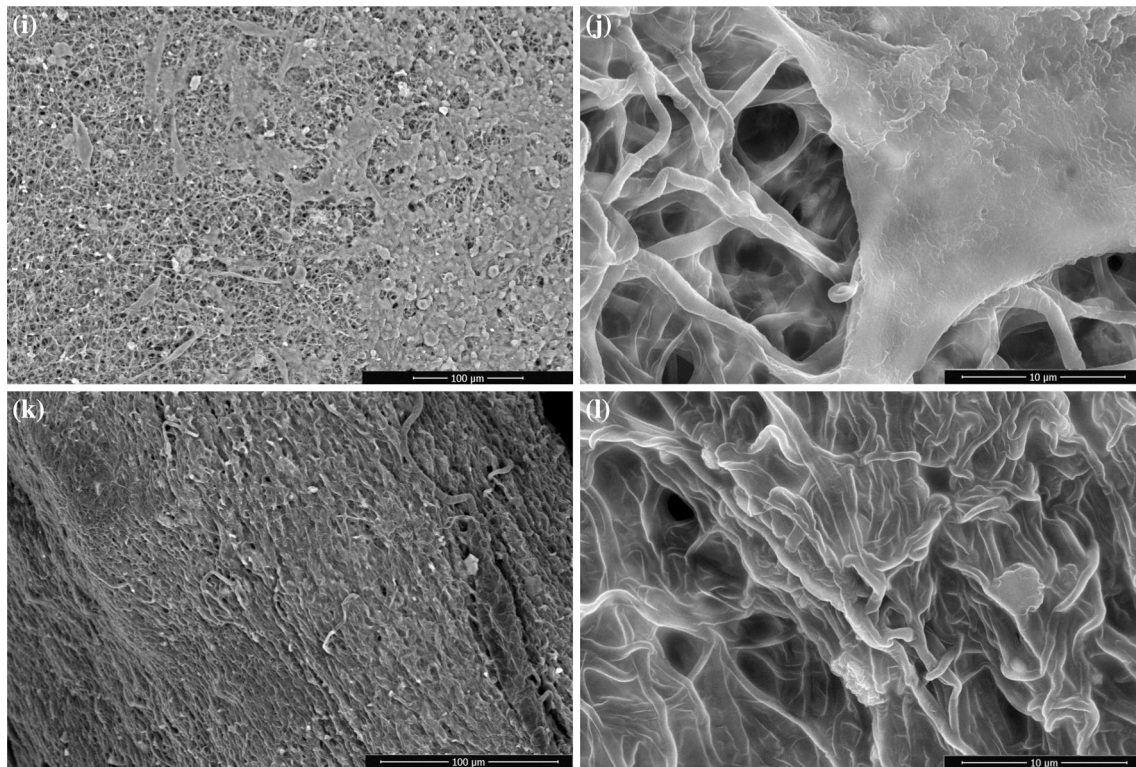
Figure 10 continued.

morphological, mechanical as well as biological features of a composite material. To further confirm this positive effect of the Mg^{2+} dopant on the mechanical properties of the composite material, Young's modulus (E) was measured as one of the parameters that should neither be too high in biological composites to cause stress shielding nor too low to collapse under stress. This modulus increased with x up to $x = 0.2$, before decreasing at higher Mg^{2+} concentrations, as it is seen in Fig. 11d. On the other hand, as seen in Fig. 11e, the maximum strain before fracture recorded its highest value of 120.03% at $x = 0.4$ and its lowest one of 70.06% at $x = 0.0$, further illustrating the improvement of the mechanical properties of the composites with doping with Mg^{2+}. This improvement in mechanical properties with the addition of Mg^{2+} to Se–CHAP is in agreement with an earlier study by Mansour et al. on co-doping CHAP with Mg^{2+} and Ag^+ and then mixing it with Chitosan, where an increase in the compressive strength up to around 15 MPa was found to result from the addition of Mg^{2+} [46].

Conclusion

Mg^{2+} ions at different amounts were incorporated successfully into Se–CHAP and the ion-doped particles were mixed into a PCL substrate and processed into $Mg_xCa_{(10-x)}(PO_4)_{5.8}(SeO_2)_{0.2}(OH)_2]/PCL$ microfibers via electrospinning. Se–CHAP lattice underwent structural changes due to doping with Mg^{2+}. Specifically, while the lattice parameter a decreased with the Mg^{2+} content up to $x = 0.3$, the lattice parameter c exhibited opposite behavior. The Mg^{2+} content in CHAP also affected the fiber dimensions, networking degree and porosity at identical weight contents of the Mg–Se–CHAP phase in PCL. Thus, while the fiber diameter was in the 2.0–2.5 μm range at $x = 0.0$, it broadened to 1.0–2.4 μm at $x = 0.5$. The fibrous scaffolds also became more networked, rougher on the surface and less porous with the addition of Mg^{2+}. All of these surface properties affected the human fibroblastic HFB4 cell response to these materials. While the cell viability tests indicated a perfectly safe response toward the cells after 3 days of exposure, the cell adhesion and proliferation improved upon the addition of Mg^{2+} to the Se–CHAP phase and infiltration into surface pores
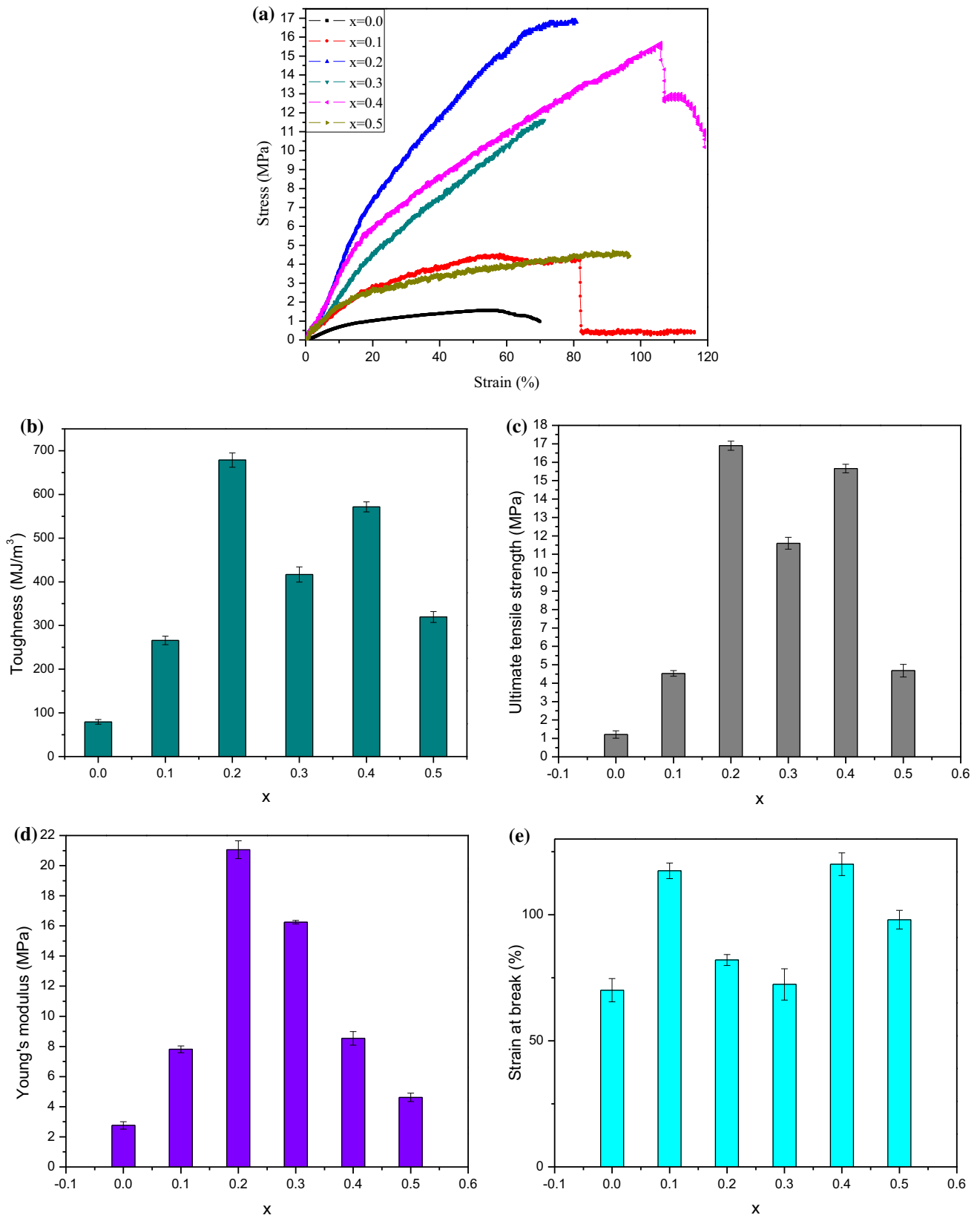
Figure 11 Dependency of mechanical properties including **a** stress–strain, **b** toughness, **c**, ultimate tensile strength, **d** Young's modulus and **e** strain at break (%) on the content of Mg^{2+} in Mg–Se–CHAP/PCL microfibers.

varied, again as a function of the Mg^{2+} content. HFB4 cells adhered and spread rapidly on the surface of the fibers and got accommodated inside the interfibrous pores, indicating a good potential for use in hard tissue engineering. The mechanical properties were also strongly affected by the Mg^{2+} content, with tensile strength, fracture toughness and elastic modulus all recording their highest values for the $x = 0.2$ composition, typically being a dozen times higher than the values recorded for the Mg-free, $x = 0$ composition. The fracture strength, for example, increased upon the addition of Mg^{2+} to Se–CHAP and peaked at 16.9 MPa for $x = 0.2$, while the maximum elongation of 120.0% was reached at $x = 0.4$. These results show that even when HAP is incorporated within a polymeric scaffold in the relatively small amount of 12 wt% and when the Mg^{2+} dopant in it is varied within a relatively narrow and low concentration window, ranging between the Mg^{2+}/Ca^{2+} molar ratios of 1:100 and 1:20, this doping may significantly affect the mechanical, morphological, microstructural and biological properties of the composite. From the practical standpoint, this novel matrix scaffold composed of Mg–Se–CHAP/PCL microfibers–notwithstanding the necessity for further optimization of different structural parameters–may improve the regeneration of repaired bone tissues and is a prospective new addendum to the list of candidates for the given biomedical application.

References

[1] Bose S, Vu AA, Emshadi K, Bandyopadhyay A (2018) Effects of polycaprolactone on alendronate drug release from Mg-doped hydroxyapatite coating on titanium. Mater Sci Eng, C 88:166–171

[2] Heshmatpour F, Lashteneshaee SH, Samadipour M (2018) Study of in vitro bioactivity of nano hydroxyapatite composites doped by various cations. J Inorg Organomet Polym Mater 28:2063–2068

[3] Wei L, Yang H, Hong J, He Z, Deng C (2018) Synthesis and structure properties of Se and Sr co-doped hydroxyapatite and their biocompatibility. J Mater Sci 54:2514–2525. https://doi.org/10.1007/s10853-018-2951-7

[4] Ahmed MK, Ramadan R, El-dek SI, Uskoković V (2019) Complex relationship between alumina and selenium-doped carbonated hydroxyapatite as the ceramic additives to

[5] Basirun WJ, Nasiri-Tabrizi B, Baradaran S (2017) Overview of hydroxyapatite-graphene nanoplatelets composite as bone graft substitute: mechanical behavior and in-vitro biofunctionality. Crit Rev Solid State Mater Sci 43:177–212

[6] Zioupos P, Currey JD (1998) Changes in the stiffness, strength, and toughness of human cortical bone with age. Bone 22:57–66

[7] Wang X, Shen X, Li X, Agrawal CM (2002) Age-related changes in the collagen network and toughness of bone. Bone 31:1–7

[8] Launey ME, Buehler MJ, Ritchie RO (2010) On the mechanistic origins of toughness in bone. Annu Rev Mater Res 40:25–53

[9] Szurkowska K, Zgadzaj A, Kuras M, Kolmas J (2018) Novel hybrid material based on Mg2 + and SiO44- co-substituted nano-hydroxyapatite, alginate and chondroitin sulphate for potential use in biomaterials engineering. Ceram Int 44:18551–18559

[10] Luo H, Xie J, Xiong L, Yang Z, Zuo G, Wang H et al (2018) Engineering photoluminescent and magnetic lamellar hydroxyapatite by facile one-step Se/Gd dual-doping. J Mater Chem B 6:3515–3521

[11] Castiglioni S, Cazzaniga A, Albisetti W, Maier JA (2013) Magnesium and osteoporosis: current state of knowledge and future research directions. Nutrients 5:3022–3033

[12] Neuman WF, Yan BJM (1971) Synthetic hydroxyapatite crystals IV magnesium incorporation. Calcif Tissue Res 7:133–138

[13] Tomazic B, Tomson M, Nancollas G (1975) Growth of calcium phosphates on hydroxyapatite crystals: the effect of magnesium. Arch Oral Biol 20:803–808

[14] Serre CM, Papillard M, Chavassieux P, Voegel JC, Boivin G (1998) Influence of magnesium substitution on a collagen–apatite biomaterial on the production of a calcifying matrix by human osteoblasts. J Biomed Mater Res 42:626–633

[15] Vecchio KS, Zhang X, Massie JB, Wang M, Kim CW (2007) Conversion of sea urchin spines to Mg-substituted tricalcium phosphate for bone implants. Acta Biomater 3:785–793

[16] Landi E, Logroscino G, Proietti L, Tampieri A, Sandri M, Sprio S (2008) Biomimetic Mg-substituted hydroxyapatite: from synthesis to in vivo behaviour. J Mater Sci Mater Med 19:239–247

[17] Kozuma W, Kon K, Kawakami S, Bobothike A, Iijima H, Shiota M, et al (2019) Osteoconductive potential of a hydroxyapatite fiber material with magnesium: In vitro and in vivo studies. Dental Mater J

electrospun polycaprolactone scaffolds for tissue engineering applications. J Alloy Compd 801:70–81

[18] Alioui H, Bouras O, Bollinger JC (2019) Toward an efficient antibacterial agent: zn- and Mg-doped hydroxyapatite nanopowders. J Environ Sci Health, Part A 54:315–327

[19] Andres NC, Sieben JM, Baldini M, Rodriguez CH, Famiglietti A, Messina PV (2018) Electroactive Mg(2 +)-hydroxyapatite nanostructured networks against drug-resistant bone infection strains. ACS Appl Mater Interfaces 10:19534–19544

[20] Menale C, Campodoni E, Palagano E, Mantero S, Erreni M, Inforzato A et al (2019) Mesenchymal stromal cell-seeded biomimetic Scaffolds as a factory of soluble RANKL in rankl-deficient osteopetrosis. Stem Cells Transl Med 8:22–34

[21] Roffi A, Kon E, Perdisa F, Fini M, Di Martino A, Parrilli A et al (2019) A composite Chitosan-reinforced scaffold fails to provide osteochondral regeneration. Int J Mol Sci 20:2227

[22] Shoeibi S, Mozdziak P, Golkar-Narenji A (2017) Biogenesis of selenium nanoparticles using green chemistry. Top Curr Chem 375:88

[23] Wang Y, Ma J, Zhou L, Chen J, Liu Y, Qiu Z et al (2012) Dual functional selenium-substituted hydroxyapatite. Interface Focus 2:378–386

[24] Zhang W, Chai Y, Cao N, Wang Y (2014) Synthesis and characterization of selenium substituted hydroxyapatite via a hydrothermal procedure. Mater Lett 134:123–125

[25] Kolmas J, Oledzka E, Sobczak M, Nalecz-Jawecki G (2014) Nanocrystalline hydroxyapatite doped with selenium oxyanions: a new material for potential biomedical applications. Mater Sci Eng C Mater Biol Appl 39:134–142

[26] Liu H, Li X, Qin F, Huang K (2014) Selenium suppresses oxidative-stress-enhanced vascular smooth muscle cell calcification by inhibiting the activation of the PI3K/AKT and ERK signaling pathways and endoplasmic reticulum stress. J Biol Inorg Chem 19:375–388

[27] Wang Y, He W, Hao H, Wu J, Qin N (2018) Eggshell derived Se-doped HA nanorods for enhanced antitumor effect and curcumin delivery. J Sol-Gel Sci Technol 87:600–607

[28] Sun J, Zheng X, Li H, Fan D, Song Z, Ma H et al (2017) Monodisperse selenium-substituted hydroxyapatite: controllable synthesis and biocompatibility. Mater Sci Eng C Mater Biol Appl 73:596–602

[29] Wei L, Pang D, He L, Deng C (2017) Crystal structure analysis of selenium-doped hydroxyapatite samples and their thermal stability. Ceram Int 43:16141–16148

[30] Gorodzha SN, Surmeneva MA, Selezneva II, Ermakov AM, Zaitsev VV, Surmenev RA (2018) Investigation of the morphology and structure of porous hybrid 3D scaffolds based on polycaprolactone involving silicate-containing hydroxyapatite. J Surf Invest 12:717–726

[31] Torres E, Fombuena V, Valles-Lluch A, Ellingham T (2017) Improvement of mechanical and biological properties of Polycaprolactone loaded with hydroxyapatite and halloysite nanotubes. Mater Sci Eng C Mater Biol Appl 75:418–424

[32] Ahmed MA, Mansour SF, El-dek SI, Abd-Elwahab SM, Ahmed MK (2014) Characterization and annealing performance of calcium phosphate nanoparticles synthesized by co-precipitation method. Ceram Int 40:12807–12820

[33] Lim SH, Liu XY, Song H, Yarema KJ, Mao HQ (2010) The effect of nanofiber-guided cell alignment on the preferential differentiation of neural stem cells. Biomaterials 31:9031–9039

[34] Srikanth M, Asmatulu R, Cluff K, Yao L (2019) Material characterization and bioanalysis of hybrid scaffolds of carbon nanomaterial and polymer nanofibers. ACS Omega 4:5044–5051

[35] Ahmed MK, Mansour SF, Mostafa MS, Darwesh R, El-dek SI (2018) Structural, mechanical and thermal features of Bi and Sr co-substituted hydroxyapatite. J Mater Sci 54:1977–1991. https://doi.org/10.1007/s10853-018-2999-4

[36] Xu HH, Weir MD, Burguera EF, Fraser AM (2006) Injectable and macroporous calcium phosphate cement scaffold. Biomaterials 27:4279–4287

[37] Mansour SF, El-dek SI, Ismail M, Ahmed MK (2018) Structure and cell viability of Pd substituted hydroxyapatite nano particles. Biomed Phys Eng Express 4:045008

[38] Safarzadeh M, Ramesh S, Tan CY, Chandran H, Noor AFM, Krishnasamy S et al (2019) Effect of multi-ions doping on the properties of carbonated hydroxyapatite bioceramic. Ceram Int 45:3473–3477

[39] Uskoković V (2015) The role of hydroxyl channel in defining selected physicochemical peculiarities exhibited by hydroxyapatite. RSC Adv 5:6614–36633

[40] Geng Z, Cui Z, Li Z, Zhu S, Liang Y, Liu Y et al (2016) Strontium incorporation to optimize the antibacterial and biological characteristics of silver-substituted hydroxyapatite coating. Mater Sci Eng C Mater Biol Appl 58:467–477

[41] Lala S, Ghosh M, Das PK, Das D, Kar T, Pradhan SK (2016) Magnesium substitution in carbonated hydroxyapatite: structural and microstructural characterization by Rietveld's refinement. Mater Chem Phys 170:319–329

[42] Sattary M, Khorasani MT, Rafienia M, Rozve HS (2018) Incorporation of nanohydroxyapatite and vitamin D3 into electrospun PCL/Gelatin scaffolds: the influence on the physical and chemical properties and cell behavior for bone tissue engineering. Polym Adv Technol 29:451–462

[43] Zhu B, Wang S, Wang L, Yang Y, Liang J, Cao B (2017) Preparation of hydroxyapatite/tannic acid coating to enhance the corrosion resistance and cytocompatibility of AZ31 magnesium alloys. Coatings 7:105

[44] Vesna M-S, Sanja E, Ana J, Maja V-S, Miodrag M, Jung YC et al (2015) Electrochemical synthesis of nanosized hydroxyapatite/graphene composite powder. Carbon Lett 16:233–240

[45] Youness RA, Taha MA, El-Kheshen AA, Ibrahim M (2018) Influence of the addition of carbonated hydroxyapatite and selenium dioxide on mechanical properties and in vitro bioactivity of borosilicate inert glass. Ceram Int 44:20677–20685

[46] Mansour SF, El-dek SI, Dorozhkin SV, Ahmed MK (2017) Physico-mechanical properties of Mg and Ag doped hydroxyapatite/chitosan biocomposites. New J Chem 41:13773–13783

[47] Lincks J, Boyan BD, Blanchard CR, Lohmann CH, Liu Y, Cochran DL et al (1998) Response of MG63 osteoblast-like cells to titanium and titanium alloy is dependent on surface roughness and composition. Biomaterials 19:2219–2232

[48] Mansour SF, El-dek SI, Ahmed MK (2017) Tailoring the structure of biphasic calcium phosphate via synthesis procedure. Mater Res Express 4:125015

[49] Shkarina S, Shkarin R, Weinhardt V, Melnik E, Vacun G, Kluger P et al (2018) 3D biodegradable scaffolds of poly-caprolactone with silicate-containing hydroxyapatite microparticles for bone tissue engineering: high-resolution tomography and in vitro study. Sci Rep 8:8907

[50] Eftekhari H, Jahandideh A, Asghari A, Akbarzadeh A, Hesaraki S (2017) Assessment of polycaprolacton (PCL) nanocomposite scaffold compared with hydroxyapatite (HA) on healing of segmental femur bone defect in rabbits. Artif Cells Nanomed Biotechnol 45:961–968

[51] Youness RA, Taha MA, Elhaes H, Ibrahim M (2017) Molecular modeling, FTIR spectral characterization and mechanical properties of carbonated-hydroxyapatite

prepared by mechanochemical synthesis. Mater Chem Phys 190:209–218

[52] Tang S, Tian B, Guo Y-J, Zhu Z-A, Guo Y-P (2014) Chitosan/carbonated hydroxyapatite composite coatings: fabrication, structure and biocompatibility. Surf Coat Technol 251:210–216

[53] Wang Y, Hao H, Zhang S (2017) Biomimetic coprecipitation of silk fibrin and calcium phosphate: influence of selenite ions. Biol Trace Elem Res 178:338–347

[54] Duta L, Mihailescu N, Popescu AC, Luculescu CR, Mihailescu IN, Çetin G et al (2017) Comparative physical, chemical and biological assessment of simple and titanium-doped ovine dentine-derived hydroxyapatite coatings fabricated by pulsed laser deposition. Appl Surf Sci 413:129–139

[55] Murugan N, Murugan C, Sundramoorthy AK (2018) In vitro and in vivo characterization of mineralized hydroxyapatite/polycaprolactone-graphene oxide based bioactive multifunctional coating on Ti alloy for bone implant applications. Arab J Chem 11:959–969

[56] Fadeeva IV, Barinov SM, Fedotov AY, Komlev VS (2012) Interactions of calcium phosphates with chitosan. Doklady Chem 441:387–390

[57] Zhang W, Xu X, Chai Y, Wang Y (2016) Synthesis and characterization of $Zn2+$ and $SeO32-$ co-substituted nano-hydroxyapatite. Adv Powder Technol 27:1857–1861

[58] Sattary M, Rafienia M, Khorasani MT, Salehi H (2018) The effect of collector type on the physical, chemical, and biological properties of polycaprolactone/gelatin/nano-hydroxyapatite electrospun scaffold. J Biomed Mater Res Part B Appl Biomat 107:933–950